

# Lithospheric Erosion in the Patagonian Slab Window, and Implications for Glacial Isostasy

Hannah Mark<sup>1</sup>, Douglas Wiens<sup>1</sup>, Erik Ivins<sup>2</sup>, Andreas Richter<sup>3</sup>, Walid Ben Mansour<sup>4</sup>, Maria Beatrice Magnani<sup>5</sup>, Eric Marderwald<sup>3</sup>, Rodrigo Adaros<sup>6</sup>, and Sergio Barrientos<sup>7</sup>

<sup>1</sup>Washington University in St Louis

<sup>2</sup>JPL

<sup>3</sup>Laboratorio MAGGIA

<sup>4</sup>Washington University in Saint Louis

<sup>5</sup>Southern Methodist University

<sup>6</sup>ENAP Magallanes

<sup>7</sup>Centro Sismológico Nacional

November 23, 2022

## Abstract

The Patagonian slab window has been proposed to enhance the solid Earth response to ice mass load changes in the overlying Northern and Southern Patagonian Icefields (NPI and SPI, respectively). Here we present the first regional seismic velocity model covering the entire north-south extent of the slab window. A slow velocity anomaly in the uppermost mantle indicates warm mantle temperature, low viscosity, and possibly partial melt. Low velocities just below the Moho suggest that the lithospheric mantle has been thermally eroded over the youngest part of the slab window. The slowest part of the anomaly is north of 49°S, implying that the NPI and the northern SPI overlie lower viscosity mantle than the southern SPI. This comprehensive seismic mapping of the slab window provides key evidence supporting the previously hypothesized connection between post-Little Ice Age anthropogenic ice mass loss and rapid geodetically observed glacial isostatic uplift ([?] 4 cm/yr).

1  
2  
3  
4  
5  
6  
7  
8  
9  
10  
11  
12  
13  
14  
15  
16  
17  
18  
19  
20

## **Lithospheric Erosion in the Patagonian Slab Window, and Implications for Glacial Isostasy**

**Hannah F. Mark<sup>1,\*†</sup>, Douglas A. Wiens<sup>1</sup>, Erik R. Ivins<sup>2</sup>, Andreas Richter<sup>3</sup>, Walid Ben Mansour<sup>1</sup>, M. Beatrice Magnani<sup>4</sup>, Eric Marderwald<sup>3</sup>, Rodrigo Adaros<sup>5</sup>, Sergio Barrientos<sup>6</sup>**

<sup>1</sup>Department of Earth and Planetary Sciences, Washington University in St. Louis; <sup>2</sup>Jet Propulsion Laboratory, California Institute of Technology; <sup>3</sup>Laboratorio MAGGIA, Universidad Nacional de La Plata; CONICET; <sup>4</sup>Southern Methodist University; <sup>5</sup>Empresa Nacional del Petróleo, Magallanes; <sup>6</sup>Centro Sismológico Nacional, Universidad de Chile

\*Corresponding author: Hannah Mark, [hmark@seismo.wustl.edu](mailto:hmark@seismo.wustl.edu)

†Now at the Woods Hole Oceanographic Institution

### **Key Points:**

- We observe anomalously low upper mantle shear wave velocities (less than 4.1 km/s) in the Patagonian slab window
- The lithospheric mantle has been thermally eroded over the youngest part of the slab window
- Low viscosities in the slab window link observed rapid geodetic uplift to geologically recent ice mass loss in Patagonia

## 21 **Abstract**

22 The Patagonian slab window has been proposed to enhance the solid Earth response to ice mass  
23 load changes in the overlying Northern and Southern Patagonian Icefields (NPI and SPI,  
24 respectively). Here we present the first regional seismic velocity model covering the entire north-  
25 south extent of the slab window. A slow velocity anomaly in the uppermost mantle indicates  
26 warm mantle temperature, low viscosity, and possibly partial melt. Low velocities just below the  
27 Moho suggest that the lithospheric mantle has been thermally eroded over the youngest part of  
28 the slab window. The slowest part of the anomaly is north of 49°S, implying that the NPI and the  
29 northern SPI overlie lower viscosity mantle than the southern SPI. This comprehensive seismic  
30 mapping of the slab window provides key evidence supporting the previously hypothesized  
31 connection between post-Little Ice Age anthropogenic ice mass loss and rapid geodetically  
32 observed glacial isostatic uplift ( $\geq 4$  cm/yr).

## 33 **Plain Language Summary**

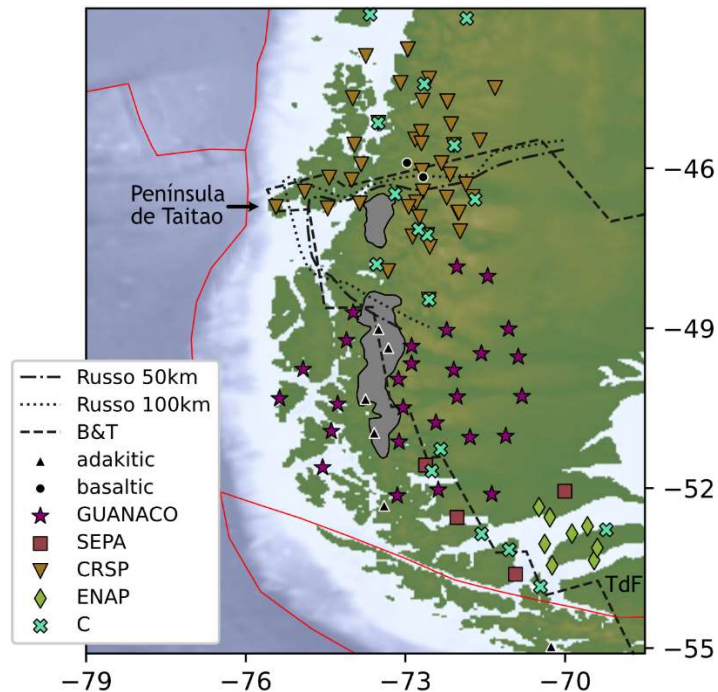
34 A gap in the subducting plate beneath Patagonia has enabled hotter, less viscous mantle material  
35 to flow underneath South America. Icefields in the Austral Andes above the gap in the plate have  
36 recently been shrinking, removing weight that had caused the continent to flex downward. We  
37 use seismic data to image the subsurface structure and find very low seismic velocity within and  
38 around the gap, as well as thinning of the rigid South American lithosphere overlying the gap.  
39 The low mantle velocity implies that mantle viscosity is also low beneath the shrinking icefields,  
40 and low viscosity enables the region to rebound upwards.

## 41 **1 Introduction**

42 Slab windows form when a spreading ridge subducts and the plates continue to diverge,  
43 opening a gap in the subducting plate interface (Groome & Thorkelson, 2009; Thorkelson,  
44 1996). Volcanic products associated with several Cenozoic slab windows can be found at  
45 subduction margins around the Pacific Ocean, indicating that this phenomenon is widespread  
46 (McCrary et al., 2009). The Patagonian slab window began forming  $\sim 18$  Ma, when the Chile  
47 Ridge started subducting beneath South America near 54°S (Breitsprecher & Thorkelson, 2009).  
48 The Chile Triple Junction (CTJ) has since migrated north to its present-day location offshore the  
49 Península de Taitao near 46.5°S. Expressions of the slab window include gaps in arc volcanism  
50 and subduction zone seismicity (Agurto-Detzel et al., 2014; DeLong et al., 1979); adakitic  
51 volcanism near slab edges (Bourgeois et al., 2016; Gorrington et al., 1997; Stern & Kilian, 1996;  
52 Thorkelson & Breitsprecher, 2005); near-trench volcanic activity (Forsythe et al., 1986; Guivel  
53 et al., 2003; Marshak & Karig, 1977); anomalously high heat flow (Ávila & Dávila, 2018; Cande  
54 et al., 1987) and low upper mantle seismic velocity (Gallego et al., 2010; Russo, VanDecar, et  
55 al., 2010); positive dynamic topography (Georgieva et al., 2016; Guillaume et al., 2009)  
56 associated with low-viscosity asthenospheric mantle upwelling (Boutonnet et al., 2010; Gorrington  
57 et al., 1997); and mantle flow patterns influenced by the slab window geometry (Murdie &  
58 Russo, 1999; Russo, Gallego, et al., 2010; Russo, VanDecar, et al., 2010). Volcanic products  
59 associated with several Cenozoic slab windows can be found at subduction margins around the  
60 Pacific Ocean, indicating that this phenomenon is widespread (McCrary et al., 2009).

61 The extent of the Patagonian slab window has previously been estimated based on plate  
62 kinematic reconstructions (Breitsprecher & Thorkelson, 2009) and has been mapped using body  
63 wave tomography in the immediate vicinity of the CTJ (Russo, VanDecar, et al., 2010). These

64 two methods are in good agreement near the CTJ (Figure 1), but the full extent of the slab  
65 window remains poorly defined. Reconciling tectonic reconstructions with observations such as  
66 the locations of slab-edge adakitic volcanism requires invoking ridge jumps and changes in  
67 spreading rates, which are poorly constrained due to the subduction of seafloor magnetic  
68 anomaly records (Bourgeois et al., 2016).  
69



70

71 **Figure 1: Map of the study region in Patagonia.** Seismic stations and volcanoes are marked.  
72 Data sources are described in Section 2. Previously estimated slab window extents are shown for  
73 Russo, VanDecar, et al. (2010) and for Breitsprecher and Thorkelson (2009). The present-day  
74 NPI and SPI are shaded in grey (Davies et al., 2020). Background map colors show bathymetry  
75 and elevation data (Ryan et al., 2009). Red lines show present-day plate boundaries. Tierra del  
76 Fuego (TdF) and the Península de Taitao are labeled.

77 The co-location of the Patagonian slab window with the Northern and Southern  
78 Patagonian Icefields (NPI and SPI) in the Austral Andes makes Patagonia an excellent place to  
79 study the effects of lateral variations in Earth structure on glacial isostatic adjustment (GIA).  
80 Low-viscosity mantle in the slab window beneath the icefields is expected to speed the GIA  
81 response to ice mass changes on decadal to centennial timescales, and ongoing glacial unloading  
82 is thought to drive extremely high uplift rates (up to 40 mm/yr) measured in the NPI and SPI  
83 (Dietrich et al., 2010; Ivins & James, 2004; Klemann et al., 2007; Lange et al., 2014; Richter et  
84 al., 2016). Improved constraints on the extent of the slab window and on lateral variations in the  
85 viscosity structure of the mantle beneath the icefields are necessary for improving GIA models  
86 and interpreting geodetic observations in terms of changing ice mass. More robust GIA models  
87 provide stronger constraints on past icefield mass and climate change (Oerlemans, 2005).

88 While surface volcanism provides some information on slab window formation and  
89 geometry, reliably reconstructing slab window mantle dynamics is a long-standing challenge in  
90 geodynamics (Dickinson, 1981; S. Lin, 2014). Seismic tomography is an essential tool for

91 connecting surface features to subsurface structure. In this study, we use seismic data recently  
92 collected by the GUANACO broadband seismic deployment to derive a new seismic velocity  
93 model for Patagonia, map the full extent of the slab window, and investigate how associated  
94 mantle dynamics have affected the overriding lithosphere. We show that the dynamics of the slab  
95 window are responsible for inferred low viscosities in the upper mantle and the unusually rapid  
96 glacial isostatic response to ice mass loss in the region.

## 97 **2 Data and methods**

98 We obtained a shear velocity ( $V_{sv}$ ) model for Patagonia by jointly inverting Rayleigh  
99 wave dispersion curves from ambient noise and earthquake tomography with P receiver  
100 functions in a Bayesian framework that enables us to quantify velocity uncertainties statistically.  
101 Data were from the GUANACO (Magnani et al., 2020), SEPA (Wiens et al., 1998), and CRSP  
102 (Russo, VanDecar, et al., 2010) temporary seismic networks; and from the Chilean National  
103 Seismic Network, the GEOSCOPE Network, the Antarctic Seismographic Argentinian Italian  
104 Network, and ENAP (Empresa Nacional del Petróleo) monitoring stations.

### 105 2.1 Rayleigh wave tomography from ambient noise and earthquake records

106 We used ambient noise tomography to obtain isotropic Rayleigh wave phase velocities at  
107 8 to 40 seconds period, and group velocities from 10 to 30 seconds (Bensen et al., 2007) (Figure  
108 S1). Temporal normalization was done with the running average method, and we incorporated  
109 time-frequency phase weighted stacking of the daily cross-correlation records (Schimmel et al.,  
110 2011; Schimmel & Gallart, 2007). We then obtained dispersion curves from the stacked cross-  
111 correlations using Automated Frequency Time Analysis (Bensen et al., 2007) and performed  
112 tomography using the method of Barmin et al. (2001). Uncertainties were estimated using a  
113 scaling relationship with ray path coverage, with group velocity uncertainties taken to be double  
114 the phase velocity uncertainties (Barmin et al., 2001; Shen et al., 2016).

115 Surface wave tomography was performed using shallow events (<50 km depth) within  
116 20-150° of the study region (Figure S2). A balanced azimuthal distribution was constructed by  
117 starting with all events with  $M_w > 6$  and adding non-overlapping events down to  $M_w$  5.4 at  
118 undersampled azimuths. We performed visual quality control on all waveforms. Helmholtz-  
119 corrected phase velocity maps were calculated from 20 to 100 seconds period using the  
120 Automated Surface-Wave Measurement System (ASWMS) (Jin & Gaherty, 2015; F.-C. Lin et  
121 al., 2009; F.-C. Lin & Ritzwoller, 2011) (Figure S3). The minimum inter-station distance for  
122 calculating cross-correlations was set to 50 km, and the maximum distance was varied with  
123 period such that it did not exceed ~4 wavelengths. The bandwidth range for the Gaussian filters  
124 applied to the waveform cross-correlations was 0.04-0.07 Hz. Automated quality controls based  
125 on the fraction of good measurements per event were intentionally relaxed for stations in the  
126 CRSP temporary network to obtain adequate data coverage near the Chile Triple Junction, and  
127 the larger velocity uncertainties near the triple junction at short periods reflect this choice.

128 Phase velocity dispersion curves from 8 to 100 seconds were constructed by combining  
129 the results from ambient noise and earthquake tomography (Figure S4). We used linear  
130 weighting across the overlapping periods, with ambient noise velocities weighted more at shorter  
131 periods and earthquake results at longer periods.

## 132 2.2 P receiver functions

133 We selected events 30-90° away from our study area with  $M_w > 5.1$  and a signal-to-noise  
134 ratio greater than 3 on the vertical component for the receiver function (RF) calculation. The  
135 seismograms were filtered from 0.33-1 Hz, and P first arrival picks were refined using STA/LTA  
136 (Withers et al., 1998) in a time window around the predicted onset time from the global model  
137 IASP91 (Kennett & Engdahl, 1991). P-to-s RFs were then calculated using the multitaper  
138 deconvolution method (Helffrich, 2006; Park et al., 1987; Park & Levin, 2000; Shibutani et al.,  
139 2008) and corrected for moveout using IASP91. For each station, a composite RF with  
140 uncertainties was obtained by taking the zeroth order component from harmonic decomposition  
141 (Bianchi et al., 2010). If azimuthal coverage was not sufficient to fit harmonics, the station  
142 average RF was used instead.

## 143 2.3 Bayesian inversion for velocity-depth models

144 We inverted for 1D velocity-depth models using a Markov chain Monte Carlo (MCMC)  
145 method (Shen et al., 2013). Each velocity-depth model was described by 14 parameters: layer  
146 thicknesses for sediments and crust; top and bottom velocities for the sediment layer; four cubic  
147 basis spline coefficients for crustal velocities; and six cubic basis spline coefficients for mantle  
148 velocities (Table S1). The total model depth was fixed at 300 km, with the lowermost 100 km of  
149 the model gradually converging to the global model AK135 (Kennett et al., 1995) since the data  
150 provide no constraints at these depths.

151 Initial prior distributions for the sediment and crustal layer thicknesses were set based on  
152 RFs. We used bootstrap stacking of H-k stacks to estimate an initial Moho depth for each station  
153 (Sandvol et al., 1998; Zhu & Kanamori, 2000). For sediment thickness, we performed a K-means  
154 clustering analysis (Pedregosa et al., 2011) on the first six seconds of the RF stacks for the  
155 stations, and used the clusters to divide the stations into those overlying “thick” sediments and  
156 “thin” sediments. The “thick” sediment cluster agreed well with the mapped extent of the  
157 Austral-Magallanes Basin (Cuitiño et al., 2019). For stations overlying “thick” sediment, the  
158 prior distribution for sediment thickness was set to  $4 \pm 4$  km, and for stations with “thin”  
159 sediment the thickness prior distribution was set to  $1 \pm 1$  km.

160 Prior distributions for velocities in all layers were set to typical values with large search  
161 ranges to allow for variation (Table S1). The sixth mantle spline coefficient at the base of our  
162 model was fixed at 4.7 km/s based on AK135, since the data have almost no sensitivity at 300  
163 km depth.

164 We imposed some velocity constraints to ensure that accepted models were physically  
165 reasonable: all velocity parameters were less than 4.9 km/s, crustal velocities were less than 4.2  
166 km/s, the velocity jump across the Moho was less than 0.7 km/s, and velocities were not allowed  
167 to decrease with depth through the sediments and crust. Dispersion curves and receiver functions  
168 were weighted equally in the joint misfit function after normalizing their respective uncertainties.  
169 We used 15 chains of 5000 steps each for the MCMC calculation. The posterior distributions for  
170 the 14 model parameters were calculated from the set of accepted models based on the misfit  
171 function (Shen et al., 2013) (Figure S5).

172 Inversions were first done for station locations. Prior distributions for the sediment and  
173 crustal layer thicknesses were then adjusted in places where the inversion failed to find a well-  
174 fitted model. This was particularly important for stations within the Austral-Magallanes Basin,

175 where the thick sediments violated the H-k stacking assumption of a constant-velocity crustal  
176 layer. We then inverted dispersion curves alone for velocity-depth model at grid points set at 0.3°  
177 intervals throughout the study area, using smoothed maps of crustal and sediment thicknesses  
178 from the station inversions to set layer thickness prior distributions.

179 The grid point and station results were combined by averaging together the 14 model  
180 parameters for each grid point with those for any stations within a 50 km radius. Weights for the  
181 station parameters were calculated based on proximity to the grid point. The model was  
182 smoothed laterally at each depth using a Gaussian filter with a standard deviation equal to the  
183 grid spacing.

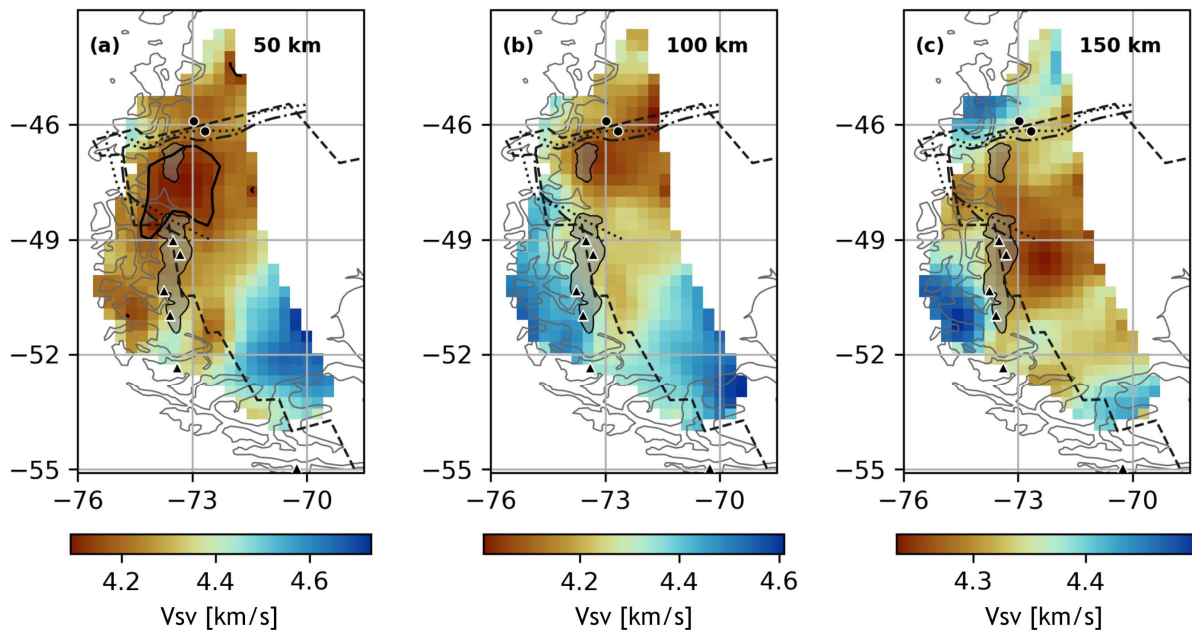
## 184 2.4 Mantle viscosity calculation

185 Although there is no direct relationship between seismic velocity and mantle viscosity,  
186 velocity is commonly used to indirectly estimate viscosity since both are largely controlled by  
187 temperature. Mantle viscosities were estimated based on differences between our velocity model  
188 and  $V_{sv}$  from the global 1D model STW105 (Kustowski et al., 2008). The seismic anomalies  
189 were used to estimate temperature anomalies relative to a global average temperature model,  
190 which were then used along with experimentally-derived flow laws to estimate deviations from a  
191 global 1D viscosity model (Ivins et al., 2021; Wu et al., 2013). We used rheologic parameters for  
192 dry diffusion creep of olivine (Hirth & Kohlstedt, 2003; Karato, 2008), a reference mantle  
193 viscosity from IJ05-R2 (Ivins et al., 2013), and temperature derivatives that included both  
194 anharmonic and anelastic contributions (Karato, 2008). The calculated viscosities would not be  
195 significantly different for wet diffusion creep given parameter uncertainties (Hirth & Kohlstedt,  
196 2003). The reference global average temperatures were calculated by proportionally weighting  
197 continental average geotherms (Stacey & Davis, 2008) and adiabatic temperature gradients  
198 beneath oceanic regions, giving 1486 K at 100 km, and 1582 K at 150 km. We set the fraction of  
199 the velocity anomaly attributed to temperature to 0.65, as found in a geodetic study of North  
200 America and Fennoscandia (Wu et al., 2013). While this temperature fraction may be different in  
201 Patagonia compared to stable cratonic regions, such variation would not change the pattern of  
202 relative viscosity differences across Patagonia. The remaining velocity anomaly is attributed to  
203 compositional variations in the mantle.

## 204 3 Results

### 205 3.1 Extent of the Patagonian slab window

206 Mantle velocities are low throughout the inferred slab window region, with a minimum  
207 velocity less than 4.1 km/s at 50 km depth, ~8% slower than the global average given by  
208 STW105 (Kustowski et al., 2008). The most intense portion of the shallow slow anomaly is north  
209 of 49°S, in the youngest part of the slab window (Figure 2). North of 51°S, the western edge of  
210 the anomaly at 100 km depth aligns with estimates of the extent of the subducting Antarctic slab  
211 from plate kinematic reconstructions (Breitsprecher & Thorkelson, 2009) and the trend of  
212 adakitic volcanism along the Austral Andes Volcanic Arc (Figure 2). Increased velocities north  
213 of Tierra del Fuego delineate the southeastern extent of the slab window effects and are  
214 consistent with xenolith studies suggesting the presence of a continental lithospheric block with  
215 thicker lithosphere (Schilling et al., 2017).



216

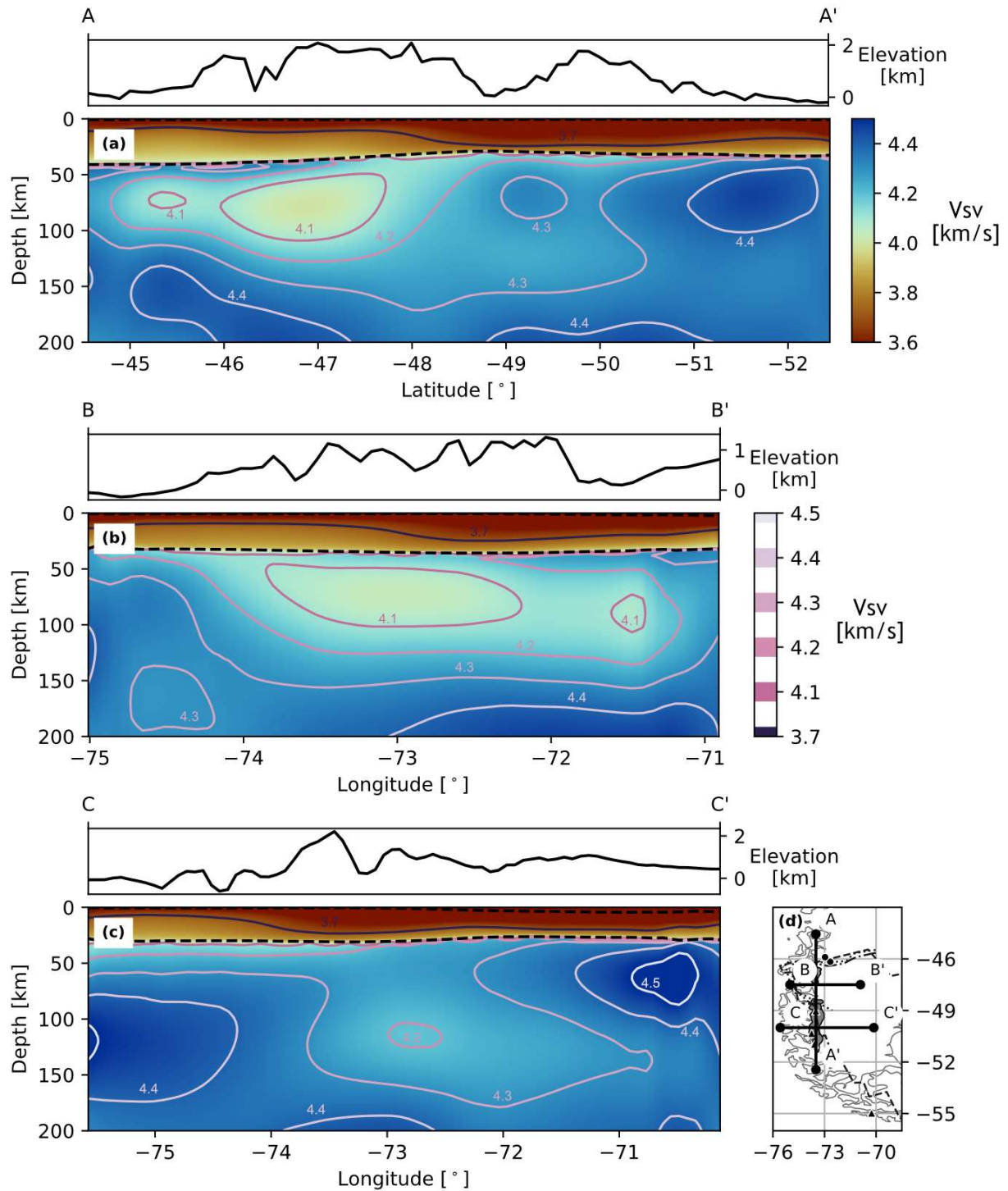
217 **Figure 2: Velocity-depth slices.** Maps show  $V_{sv}$  in km/s: **(a)** 50 km depth, contour at 4.15 km/s  
218 (solid black line); **(b)** 100 km depth; **(c)** 150 km depth. Other lines and symbols are as in Figure  
219 1. Velocity uncertainties are  $\sim 0.1$  km/s across most of the maps; velocity uncertainty maps are  
220 shown in Figure S6.

221

### 3.2 Thermal erosion of the South American lithosphere

222

223 Velocities directly beneath the crust near the CTJ are much lower than expected for  
224 continental lithosphere (4.1 km/s at 50 km, compared to 4.5 km/s for STW105; Kustowski et al.,  
225 2008), indicating that the lithospheric mantle is missing in the youngest part of the slab window  
226 (Figure 2a). Vertical cross sections through the slab window show that anomalously slow mantle  
227 velocities are present immediately below the Moho, with thin ( $< 10$  km thick) patches of faster  
mantle material at the Moho in places (Figure 3a, 45 to 47°S).



228

229 **Figure 3: Velocity cross sections.** Cross sections show  $V_{sv}$  along (a) 73.5°W, (b) 47.5°S, and (c)  
230 50°S, with transect locations shown on a map (d). Other lines and symbols on the map are as in  
231 Figure 1. Topography over each transect is plotted above the velocities (Ryan et al., 2009).  
232 Dashed black lines mark the base of the sediments and the Moho on each cross section, and

233 labeled lines show isovelocity contours. The  $V_{sv}$  color scale is saturated at 3.6 km/s on the low  
234 end to emphasize slow anomalies in the mantle.

235 The absence of lithospheric mantle near the CTJ suggests that mantle dynamics  
236 associated with the slab window have eroded the base of the plate. Thermal erosion of the  
237 overriding plate is predicted by thermo-mechanical models of ridge subduction (Groome &  
238 Thorkelson, 2009), and shallow slow velocity anomalies beneath the Antarctic Peninsula have  
239 been similarly interpreted (Lloyd et al., 2020). Previous studies have inferred that the Patagonian  
240 lithosphere has thinned above the slab window based on regional heat flow data (Ávila & Dávila,  
241 2018), crustal thickness measurements (Robertson Maurice et al., 2003), and GIA models fit to  
242 observed uplift rates (Lange et al., 2014; Richter et al., 2016).

243 The process of thermal erosion likely requires the presence of melt or fluids, as purely  
244 conductive heating is too slow relative to the age of the slab window. In the absence of a present-  
245 day slab and slab-derived volatiles, melt may be supplied by decompression of upwelling  
246 asthenospheric mantle. There are no known active Holocene volcanos over the slowest part of  
247 the velocity anomaly, but the presence of the icefields complicates the mapping of volcanic  
248 activity. Shear wave splitting analyses show a strong E–W fast direction near the CTJ, indicating  
249 vigorous mantle flow around the edge of the Nazca slab (Russo, Gallego, et al., 2010; Russo,  
250 VanDecar, et al., 2010; Wiens et al., 2021), and fast mantle flow in the shallow asthenosphere  
251 may assist in the removal of lithospheric material.

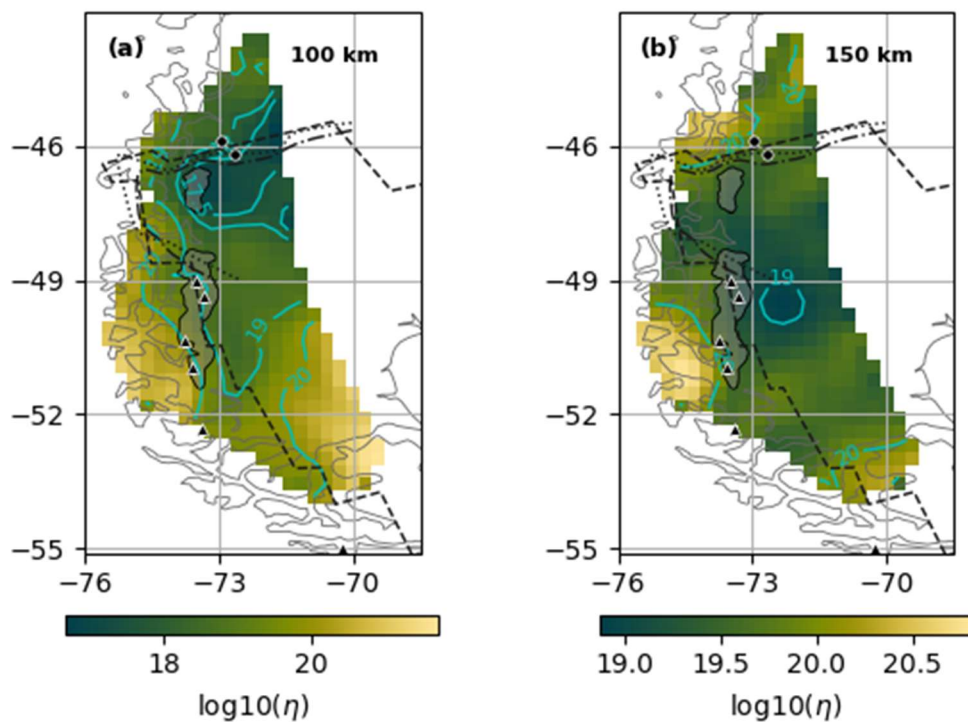
252 Lithospheric erosion near the CTJ contrasts with the structure farther south, where fast  
253 velocities indicate that the lithospheric mantle is largely intact beneath the Austral-Magallanes  
254 Basin. Patagonia has a complex history of terrane accretion (Ramos & Ghiglione, 2008), and it is  
255 possible that the lithosphere in the south was thicker prior to the opening of the slab window.  
256 Alternatively, thermal erosion may have been less efficient during the earliest stages of ridge  
257 subduction, becoming more efficient over time as the slab window thermally perturbed the  
258 surrounding mantle. As ridge subduction initiated only 18 Ma and subsequent ridge segments  
259 entered the trench at ~12 Ma, 6 Ma, and 3 Ma, we expect that timescales of conductive cooling  
260 are too short relative to the age of the slab window to allow for significant re-formation of  
261 mantle lithosphere even in the oldest parts of the window (Boutonnet et al., 2010).

262 The crust thins by >10 km from north to south over the slab window (Figure 3, S7, S8).  
263 This trend is opposite the lithospheric erosion seen at the Moho, and is unlikely to be entirely due  
264 to surface erosion since the thinning is not primarily in the upper crust. Along the west coast of  
265 North America, the passage of the migrating Mendocino Triple Junction is thought to have  
266 caused rapid, temporary crustal thickening followed by crustal thinning (Furlong & Govers,  
267 1999). The same mechanism may be at work in Patagonia, but the trend of mean relief along the  
268 Austral Andes does not match predictions for flexural downwarping associated with this model  
269 for crustal modification (Georgieva et al., 2016). Preexisting structure, overthrusting of terranes,  
270 thermal erosion, and tectonic extension have also been proposed to explain crustal structure near  
271 the CTJ (Rodríguez & Russo, 2020), and further measurements extending north of our study  
272 region would help clarify the source of the variations in crustal thickness.

#### 273 **4 Implications for glacial isostatic adjustment**

274 Mantle viscosity structure strongly controls GIA, which in turn responds to spatial and  
275 temporal ice-mass variations. High geodetic uplift rates around the NPI and SPI ( $\geq 4$  cm/yr) have

276 been attributed to anomalous mantle viscosities lower than  $2 \times 10^{18}$  Pa s (Ivins & James, 2004;  
277 Lange et al., 2014; Richter et al., 2016), and recent GIA models suggest that reproducing  
278 observed uplift rates requires either mantle viscosities that are significantly lower beneath the  
279 NPI compared to the SPI or more ice mass loss in the NPI than previously estimated (Lange et  
280 al., 2014; Russo et al., 2021). The observed location of the slowest part of the seismic velocity  
281 anomaly north of  $49^\circ\text{S}$  is consistent with the former explanation, and viscosities estimated from  
282 our velocity model also point to both low overall viscosity in the slab window and a difference in  
283 structure beneath the two icefields (Figure 4). Our estimated viscosities are mostly higher than  
284 the values obtained by previous geodetic studies (Lange et al., 2014; Richter et al., 2016), but we  
285 emphasize that the absolute viscosity values we obtain are highly sensitive to uncertain  
286 parameters such as the fraction of velocity variation due to temperature. The extent of the slow  
287 anomaly also suggests that gradients in uplift rates along the SPI may reflect latitudinal variation  
288 in mantle viscosity. In broader terms, the strong lateral heterogeneity in mantle viscosity  
289 indicated by the velocity model implies that the geodetic response to glacial unloading in  
290 Patagonia will be highly three-dimensional, and cannot be fully described by symmetric  
291 deformation predicted for a radially layered mantle, particularly with respect to the prediction of  
292 horizontal crustal motions (Klemann et al., 2007).  
293



294

295 **Figure 4: Estimated mantle viscosity based on the seismic velocity model.** Maps of  $\log_{10}(\eta)$  at  
296 (a) 100 km and (b) 150 km depth. Other lines and symbols on the map are as described in the  
297 captions for Figures 1 and 2.

298 The patterns of lithospheric erosion and thinning observed in our velocity model are also  
299 expected to affect GIA. While the seismic lithosphere is not exactly equivalent to the elastic  
300 lithosphere relevant to geodetic models, both terms refer to a layer of colder, more rigid material

301 that acts as a lowpass filter on the response of the mantle to changes in surface loading. The thin  
302 lithosphere observed near the CTJ enables shorter wavelength signals from GIA loading and  
303 mantle viscosity variations to be observed in surface deformation and topography. In the south,  
304 the fast velocities to the east indicate that thicker continental lithospheric mantle beneath the  
305 Austral-Magallanes Basin may constrain mantle flow patterns in the older parts of the slab  
306 window by blocking shallow latitudinal flow (Klemann et al., 2007). In this scenario, horizontal  
307 surface motions on the eastern side of the SPI are predicted to be dominantly to the east, and  
308 GNSS observations of horizontal surface displacements support this prediction where data are  
309 available along the eastern side of the northern SPI (Richter et al., 2016).

310 Quantifying ice mass changes on the Patagonian Icefields is crucial for projecting future  
311 water resources and informing models of global sea level rise. Temperate mountain glaciers  
312 including the NPI and SPI currently contribute substantially to global mean sea level rise (Jacob  
313 et al., 2012; Radić & Hock, 2011). Ice and hydrological mass changes are efficiently monitored  
314 by satellite gravimetry, provided the GIA gravity effect is accurately removed (Ivins et al.,  
315 2011). However, there are large trade-offs in GIA modeling between ice mass history and mantle  
316 viscosity structure (Lange et al., 2014), so uncertainties in mantle viscosity propagate forward  
317 into highly uncertain ice mass change rates (Richter et al., 2019). Constraining the regional 3D  
318 viscosity structure provides the space gravimetry community with key information on the solid  
319 Earth contribution to the secular mass change signal in Patagonia.

320 The geologically rapid response of Patagonian topography to ice mass changes makes the  
321 area above the slab window ideal for studying the connections between the solid Earth rheology  
322 and dynamics, surface processes, and climate. The heterogeneous mantle structure indicated by  
323 seismic velocities implies that the isostatic response to ice mass changes will also be  
324 heterogeneous, and the absence of mantle lithosphere over the slab window promotes the  
325 observation of shorter wavelength variations in surface deformation. Lateral heterogeneity in  
326 mantle viscosity and lithospheric thickness, guided by seismic models and other geophysical  
327 observations, must be incorporated into GIA modeling in this region. The resulting higher  
328 quality models will help advance our understanding of the history and the future of the  
329 cryosphere and hydrosphere in Patagonia.

### 330 **Acknowledgments**

331 We thank Patrick Shore, Gerardo Connon, Leticia Duca, Celeste Bollini, Nora Sabbione,  
332 Gerd Sielfeld, Daniel Valladares, and many others for their work in planning, deploying,  
333 servicing, and recovering the GUANACO seismic array. We also thank Maeva Pourpoint for her  
334 work in the field and with initial data processing; Weisen Shen for sharing his Bayesian  
335 inversion code; and Zhengyang Zhou and Zongshan Li for their help with several of the software  
336 packages used for data processing. We thank reviewers R. M. Russo and Volker Klemann for  
337 their thoughtful comments. The OCCAP Foundation assisted in arranging boat transport to  
338 remote stations in Chile. ENAP Magallanes provided additional seismic data. The seismic  
339 instruments were provided by the IRIS-PASSCAL Instrument Center at New Mexico Tech. The  
340 facilities of the IRIS Consortium are supported by the National Science Foundation's SAGE  
341 Award under Cooperative Support Agreement EAR-1851048. The GUANACO project is funded  
342 by the National Science Foundation under grants EAR-1714154 to WUSTL and EAR-1714662  
343 to SMU, and E. R. I. was supported by NASA under grant NNH19ZDA001N-GRACEFO.

## 344 Open Research

345 Data used in this study is from the GUANACO, SEPA, and CRSP temporary seismic  
346 networks (network codes: 1P, 10/2018-03/2021; XB, 02/1997-10/1998; YJ, 12/2004-12/2006),  
347 permanent stations from the Chile Network, GEOSCOPE, and the Antarctic Seismographic  
348 Argentinian Italian Network (network codes: C, C1, G, AI), and stations operated and  
349 maintained by ENAP. Data for all except the ENAP stations can be obtained from the IRIS DMC  
350 (<https://ds.iris.edu/ds/nodes/dmc>). The earthquake records and ambient noise cross-correlations  
351 for ENAP stations used in this study are publicly available (Mark et al., 2021a,  
352 <https://doi.org/10.5281/zenodo.5508198>). The final velocity and viscosity models presented in  
353 this paper are also available (Mark et al., 2021b, <https://doi.org/10.5281/zenodo.5794167>).

354 Publicly released versions of the codes used for analysis can be found at:  
355 <https://github.com/NoiseCIEI/Seed2Cor>, <https://github.com/NoiseCIEI/AFTAN>,  
356 <https://github.com/NoiseCIEI/RayTomo>, <https://github.com/trichter/rtf>,  
357 <https://github.com/jinwar/matgsdf>, and  
358 <http://diapiro.ictja.csic.es/gt/mschi/SCIENCE/tseries.html#software>. These codes are currently  
359 only available on github and researchers' personal websites. Color palettes for all figures are  
360 from Fabio Cramerì's ScientificColourMaps7 (<https://doi.org/10.5281/zenodo.1243862>).

## 361 References

- 362 Agurto-Detzel, H., Rietbrock, A., Bataille, K., Miller, M., Iwamori, H., & Priestley, K. (2014).  
363 Seismicity distribution in the vicinity of the Chile Triple Junction, Aysén Region,  
364 southern Chile. *Journal of South American Earth Sciences*, *51*, 1–11.  
365 <https://doi.org/10.1016/j.jsames.2013.12.011>
- 366 Ávila, P., & Dávila, F. M. (2018). Heat flow and lithospheric thickness analysis in the  
367 Patagonian asthenospheric windows, southern South America. *Tectonophysics*, *747–748*,  
368 99–107. <https://doi.org/10.1016/j.tecto.2018.10.006>
- 369 Barmin, M. P., Ritzwoller, M. H., & Levshin, A. L. (2001). A Fast and Reliable Method for  
370 Surface Wave Tomography. *Pure Appl. Geophys.*, *158*, 25.
- 371 Bensen, G. D., Ritzwoller, M. H., Barmin, M. P., Levshin, A. L., Lin, F., Moschetti, M. P., et al.  
372 (2007). Processing seismic ambient noise data to obtain reliable broad-band surface wave  
373 dispersion measurements. *Geophysical Journal International*, *169*(3), 1239–1260.  
374 <https://doi.org/10.1111/j.1365-246X.2007.03374.x>
- 375 Bianchi, I., Park, J., Piana Agostinetti, N., & Levin, V. (2010). Mapping seismic anisotropy  
376 using harmonic decomposition of receiver functions: An application to Northern  
377 Apennines, Italy. *Journal of Geophysical Research*, *115*(B12), B12317.  
378 <https://doi.org/10.1029/2009JB007061>
- 379 Bourgois, J., Lagabrielle, Y., Martin, H., Dymant, J., Frutos, J., & Cisternas, M. E. (2016). A  
380 Review on Forearc Ophiolite Obduction, Adakite-Like Generation, and Slab Window  
381 Development at the Chile Triple Junction Area: Uniformitarian Framework for  
382 Spreading-Ridge Subduction. *Pure and Applied Geophysics*, *173*(10–11), 3217–3246.  
383 <https://doi.org/10.1007/s00024-016-1317-9>
- 384 Boutonnet, E., Arnaud, N., Guivel, C., Lagabrielle, Y., Scalabrino, B., & Espinoza, F. (2010).  
385 Subduction of the South Chile active spreading ridge: A 17Ma to 3Ma magmatic record

- 386 in central Patagonia (western edge of Meseta del Lago Buenos Aires, Argentina). *Journal*  
387 *of Volcanology and Geothermal Research*, 189(3–4), 319–339.  
388 <https://doi.org/10.1016/j.jvolgeores.2009.11.022>
- 389 Breitsprecher, K., & Thorkelson, D. J. (2009). Neogene kinematic history of Nazca–Antarctic–  
390 Phoenix slab windows beneath Patagonia and the Antarctic Peninsula. *Tectonophysics*,  
391 464(1–4), 10–20. <https://doi.org/10.1016/j.tecto.2008.02.013>
- 392 Cande, S. C., Leslie, R. B., Parra, J. C., & Hobart, M. (1987). Interaction between the Chile  
393 Ridge and Chile Trench: Geophysical and geothermal evidence. *Journal of Geophysical*  
394 *Research*, 92(B1), 495. <https://doi.org/10.1029/JB092iB01p00495>
- 395 Cuitiño, J. I., Varela, A. N., Ghiglione, M. C., Richiano, S., & Poiré, D. G. (2019). The Austral-  
396 Magallanes Basin (Southern Patagonia): A Synthesis of its Stratigraphy and Evolution.  
397 *Latin American Journal of Sedimentology and Basin Analysis*, 26(2), 12.
- 398 Davies, B., Darvill, C., Lovell, H., Bendle, J., Dowdeswell, J., Fabel, D., et al. (2020). Data for:  
399 The evolution of the Patagonian Ice Sheet from 35 ka to the Present Day (PATICE), 1.  
400 <https://doi.org/10.17632/ztz59y79vv.1>
- 401 DeLong, S. E., Schwarz, W. M., & Anderson, R. N. (1979). Thermal effects of ridge subduction.  
402 *Earth and Planetary Science Letters*, 44(2), 239–246. [https://doi.org/10.1016/0012-](https://doi.org/10.1016/0012-821X(79)90172-9)  
403 821X(79)90172-9
- 404 Dickinson, W. R. (1981). Plate tectonics of the continental margin of California. In W. G. Ernst  
405 (Ed.), *The Geotectonic Development of California (Rubey)* (Vol. 1, pp. 1–28). Prentice  
406 Hall.
- 407 Dietrich, R., Ivins, E. R., Casassa, G., Lange, H., Wendt, J., & Fritsche, M. (2010). Rapid crustal  
408 uplift in Patagonia due to enhanced ice loss. *Earth and Planetary Science Letters*, 289(1–  
409 2), 22–29. <https://doi.org/10.1016/j.epsl.2009.10.021>
- 410 Forsythe, R. D., Nelson, E. P., Carr, M. J., Kaeding, M. E., Herve, M., Mpodozis, C., et al.  
411 (1986). Pliocene near-trench magmatism in southern Chile: A possible manifestation of  
412 ridge collision. *Geology*, 14, 5.
- 413 Furlong, K. P., & Govers, R. (1999). Ephemeral crustal thickening at a triple junction: The  
414 Mendocino crustal conveyor. *Geology*, 27(2), 4.
- 415 Gallego, A., Russo, R. M., Comte, D., Mocanu, V. I., Murdie, R. E., & Vandecar, J. C. (2010).  
416 Seismic noise tomography in the Chile ridge subduction region. *Geophysical Journal*  
417 *International*, 182(3), 1478–1492. <https://doi.org/10.1111/j.1365-246X.2010.04691.x>
- 418 Georgieva, V., Melnick, D., Schildgen, T. F., Ehlers, T. A., Lagabriele, Y., Enkelmann, E., &  
419 Strecker, M. R. (2016). Tectonic control on rock uplift, exhumation, and topography  
420 above an oceanic ridge collision: Southern Patagonian Andes (47°S), Chile: Neotectonics  
421 and Topography in Patagonia. *Tectonics*, 35(6), 1317–1341.  
422 <https://doi.org/10.1002/2016TC004120>
- 423 Gorrington, M. L., Kay, S. M., Zeitler, P. K., Ramos, V. A., Rubiolo, D., Fernandez, M. I., & Panza,  
424 J. L. (1997). Neogene Patagonian plateau lavas: Continental magmas associated with  
425 ridge collision at the Chile Triple Junction. *Tectonics*, 16(1), 1–17.  
426 <https://doi.org/10.1029/96TC03368>

- 427 Groome, W. G., & Thorkelson, D. J. (2009). The three-dimensional thermo-mechanical signature  
428 of ridge subduction and slab window migration. *Tectonophysics*, 464(1–4), 70–83.  
429 <https://doi.org/10.1016/j.tecto.2008.07.003>
- 430 Guillaume, B., Martinod, J., Husson, L., Roddaz, M., & Riquelme, R. (2009). Neogene uplift of  
431 central eastern Patagonia: Dynamic response to active spreading ridge subduction?  
432 *Tectonics*, 28(2). <https://doi.org/10.1029/2008TC002324>
- 433 Guivel, C., Lagabrielle, Y., Bourgois, J., Martin, H., Arnaud, N., Fourcade, S., et al. (2003).  
434 Very shallow melting of oceanic crust during spreading ridge subduction: Origin of near-  
435 trench Quaternary volcanism at the Chile Triple Junction. *Journal of Geophysical*  
436 *Research: Solid Earth*, 108(B7). <https://doi.org/10.1029/2002JB002119>
- 437 Helffrich, G. (2006). Extended-Time Multitaper Frequency Domain Cross-Correlation Receiver-  
438 Function Estimation. *Bulletin of the Seismological Society of America*, 96(1), 344–347.  
439 <https://doi.org/10.1785/0120050098>
- 440 Hirth, G., & Kohlstedt, D. (2003). Rheology of the Upper Mantle and the Mantle Wedge: A  
441 View from the Experimentalists. In J. Eiler (Ed.), *Inside the Subduction Factory* (pp. 83–  
442 105). American Geophysical Union. <https://doi.org/10.1029/138GM06>
- 443 Ivins, E. R., & James, T. S. (2004). Bedrock response to Llanquihue Holocene and present-day  
444 glaciation in southernmost South America. *Geophysical Research Letters*, 31(24),  
445 L24613. <https://doi.org/10.1029/2004GL021500>
- 446 Ivins, E. R., Watkins, M. M., Yuan, D.-N., Dietrich, R., Casassa, G., & Rülke, A. (2011). On-  
447 land ice loss and glacial isostatic adjustment at the Drake Passage: 2003–2009. *Journal of*  
448 *Geophysical Research*, 116(B2), B02403. <https://doi.org/10.1029/2010JB007607>
- 449 Ivins, E. R., James, T. S., Wahr, J., O. Schrama, E. J., Landerer, F. W., & Simon, K. M. (2013).  
450 Antarctic contribution to sea level rise observed by GRACE with improved GIA  
451 correction. *Journal of Geophysical Research: Solid Earth*, 118(6), 3126–3141.  
452 <https://doi.org/10.1002/jgrb.50208>
- 453 Ivins, E. R., Wal, W. van der, Wiens, D. A., Lloyd, A. J., & Caron, L. (2021). Antarctic Upper  
454 Mantle Rheology. *Geological Society, London, Memoirs*, 56.  
455 <https://doi.org/10.1144/M56-2020-19>
- 456 Jacob, T., Wahr, J., Pfeffer, W. T., & Swenson, S. (2012). Recent contributions of glaciers and  
457 ice caps to sea level rise. *Nature*, 482(7386), 514–518.  
458 <https://doi.org/10.1038/nature10847>
- 459 Jin, G., & Gaherty, J. B. (2015). Surface wave phase-velocity tomography based on multichannel  
460 cross-correlation. *Geophysical Journal International*, 16.
- 461 Karato, S. (2008). Deformation of earth materials. *An Introduction to the Rheology of Solid*  
462 *Earth*, 463.
- 463 Kennett, B. L. N., & Engdahl, E. R. (1991). Traveltimes for global earthquake location and phase  
464 identification. *Geophysical Journal International*, 105(2), 429–465.  
465 <https://doi.org/10.1111/j.1365-246X.1991.tb06724.x>
- 466 Kennett, B. L. N., Engdahl, E. R., & Buland, R. (1995). Constraints on seismic velocities in the  
467 Earth from traveltimes. *Geophysical Journal International*, 122(1), 108–124.

- 468 Klemann, V., Ivins, E. R., Martinec, Z., & Wolf, D. (2007). Models of active glacial isostasy  
469 roofing warm subduction: Case of the South Patagonian Ice Field. *Journal of*  
470 *Geophysical Research*, *112*(B9), B09405. <https://doi.org/10.1029/2006JB004818>
- 471 Kustowski, B., Ekström, G., & Dziewoński, A. M. (2008). Anisotropic shear-wave velocity  
472 structure of the Earth's mantle: A global model. *Journal of Geophysical Research*,  
473 *113*(B6), B06306. <https://doi.org/10.1029/2007JB005169>
- 474 Lange, H., Casassa, G., Ivins, E. R., Schröder, L., Fritsche, M., Richter, A., et al. (2014).  
475 Observed crustal uplift near the Southern Patagonian Icefield constrains improved  
476 viscoelastic Earth models. *Geophysical Research Letters*, *41*(3), 805–812.  
477 <https://doi.org/10.1002/2013GL058419>
- 478 Lin, F.-C., & Ritzwoller, M. H. (2011). Helmholtz surface wave tomography for isotropic and  
479 azimuthally anisotropic structure. *Geophysical Journal International*, *186*(3), 1104–1120.  
480 <https://doi.org/10.1111/j.1365-246X.2011.05070.x>
- 481 Lin, F.-C., Ritzwoller, M. H., & Snieder, R. (2009). Eikonal tomography: surface wave  
482 tomography by phase front tracking across a regional broad-band seismic array.  
483 *Geophysical Journal International*, *177*(3), 1091–1110. <https://doi.org/10.1111/j.1365-246X.2009.04105.x>
- 485 Lin, S. (2014). Three-dimensional mantle circulations and lateral slab deformation in the  
486 southern Chilean subduction zone. *Journal of Geophysical Research: Solid Earth*,  
487 *119*(4), 3879–3896. <https://doi.org/10.1002/2013JB010864>
- 488 Lloyd, A. J., Wiens, D. A., Zhu, H., Tromp, J., Nyblade, A. A., Aster, R. C., et al. (2020).  
489 Seismic Structure of the Antarctic Upper Mantle Imaged with Adjoint Tomography.  
490 *Journal of Geophysical Research: Solid Earth*, *125*(3), 2019JB017823.  
491 <https://doi.org/10.1029/2019JB017823>
- 492 Magnani, M. B., Ito, E., Wiens, D., Wickert, A. D., Ivins, E. R., Fedotova, A., et al. (2020). Solid  
493 Earth response of the Patagonian Andes to post-Little Ice Age glacial retreat: a multi-  
494 pronged approach. *AGU Fall Meeting Abstracts, 2020*, G013-05.
- 495 Mark, H. F., Wiens, D. A., Ivins, E. R., Richter, A., Ben Mansour, W., Magnani, M. B., et al.  
496 (2021a). Earthquake records and ambient noise cross correlations from ENAP  
497 Magallanes seismographs, Jan 2019- Mar 2020 [Data set]. Zenodo.  
498 <https://doi.org/10.5281/zenodo.5508198>
- 499 Mark, H. F., Wiens, D. A., Ivins, E. R., Richter, A., Ben Mansour, W., Magnani, M. B., et al.  
500 (2021b). Velocity and viscosity models for southern Patagonia, from the GUANACO  
501 experiment [Data set]. Zenodo. <https://doi.org/10.5281/zenodo.5794167>
- 502 Marshak, R. S., & Karig, D. E. (1977). Triple junctions as a cause for anomalously near-trench  
503 igneous activity between the trench and volcanic arc. *Geology*, *5*(4), 233–236.  
504 [https://doi.org/10.1130/0091-7613\(1977\)5<233:TJAACF>2.0.CO;2](https://doi.org/10.1130/0091-7613(1977)5<233:TJAACF>2.0.CO;2)
- 505 McCrory, P. A., Wilson, D. S., & Stanley, R. G. (2009). Continuing evolution of the Pacific–  
506 Juan de Fuca–North America slab window system—A trench–ridge–transform example  
507 from the Pacific Rim. *Tectonophysics*, *464*(1–4), 30–42.  
508 <https://doi.org/10.1016/j.tecto.2008.01.018>

- 509 Murdie, R. E., & Russo, R. M. (1999). Seismic anisotropy in the region of the Chile margin  
510 triple junction. *Journal of South American Earth Sciences*, 12(3), 261–270.  
511 [https://doi.org/10.1016/S0895-9811\(99\)00018-8](https://doi.org/10.1016/S0895-9811(99)00018-8)
- 512 Oerlemans, J. (2005). Extracting a Climate Signal from 169 Glacier Records. *Science*,  
513 308(5722), 675–677. <https://doi.org/10.1126/science.1107046>
- 514 Park, J., & Levin, V. (2000). Receiver Functions from Multiple-Taper Spectral Correlation  
515 Estimates. *Bulletin of the Seismological Society of America*, 90(6), 1507–1520.  
516 <https://doi.org/10.1785/0119990122>
- 517 Park, J., Lindberg, C. R., & Vernon, F. L. (1987). Multitaper spectral analysis of high-frequency  
518 seismograms. *Journal of Geophysical Research: Solid Earth*, 92(B12), 12675–12684.  
519 <https://doi.org/10.1029/JB092iB12p12675>
- 520 Pedregosa, F., Varoquaux, G., Gramfort, A., Michel, V., Thirion, B., Grisel, O., et al. (2011).  
521 Scikit-learn: Machine Learning in Python. *Journal of Machine Learning Research*, 12,  
522 2825–2830.
- 523 Radić, V., & Hock, R. (2011). Regionally differentiated contribution of mountain glaciers and  
524 ice caps to future sea-level rise. *Nature Geoscience*, 4(2), 91–94.  
525 <https://doi.org/10.1038/ngeo1052>
- 526 Ramos, V. A., & Ghiglione, M. C. (2008). Tectonic Evolution of the Patagonian Andes. In  
527 *Developments in Quaternary Sciences* (Vol. 11, pp. 57–71). Elsevier.  
528 [https://doi.org/10.1016/S1571-0866\(07\)10004-X](https://doi.org/10.1016/S1571-0866(07)10004-X)
- 529 Richter, A., Ivins, E. R., Lange, H., Mendoza, L., Schröder, L., Hormaechea, J. L., et al. (2016).  
530 Crustal deformation across the Southern Patagonian Icefield observed by GNSS. *Earth  
531 and Planetary Science Letters*, 452, 206–215. <https://doi.org/10.1016/j.epsl.2016.07.042>
- 532 Richter, A., Groh, A., Horwath, M., Ivins, E. R., Marderwald, E., Hormaechea, J. L., et al.  
533 (2019). The Rapid and Steady Mass Loss of the Patagonian Icefields throughout the  
534 GRACE Era: 2002–2017. *Remote Sensing*, 11(8), 909.  
535 <https://doi.org/10.3390/rs11080909>
- 536 Robertson Maurice, S. D., Wiens, D. A., Koper, K. D., & Vera, E. (2003). Crustal and upper  
537 mantle structure of southernmost South America inferred from regional waveform  
538 inversion. *Journal of Geophysical Research: Solid Earth*, 108(B1).  
539 <https://doi.org/10.1029/2002JB001828>
- 540 Rodriguez, E. E., & Russo, R. M. (2020). Southern Chile crustal structure from teleseismic  
541 receiver functions: Responses to ridge subduction and terrane assembly of Patagonia.  
542 *Geosphere*, 16(1), 378–391. <https://doi.org/10.1130/GES01692.1>
- 543 Russo, R. M., Gallego, A., Comte, D., Mocanu, V. I., Murdie, R. E., & VanDecar, J. C. (2010).  
544 Source-side shear wave splitting and upper mantle flow in the Chile Ridge subduction  
545 region. *Geology*, 38(8), 707–710. <https://doi.org/10.1130/G30920.1>
- 546 Russo, R. M., VanDecar, J. C., Comte, D., Mocanu, V. I., Gallego, A., & Murdie, R. E. (2010).  
547 Subduction of the Chile Ridge: Upper mantle structure and flow. *GSA Today*, 4–10.  
548 <https://doi.org/10.1130/GSATG61A.1>

- 549 Russo, R. M., Luo, H., Wang, K., Ambrosius, B., Mocanu, V., He, J., et al. (2021). Lateral  
550 variation in slab window viscosity inferred from global navigation satellite system  
551 (GNSS)–observed uplift due to recent mass loss at Patagonia ice fields. *Geology*.  
552 <https://doi.org/10.1130/G49388.1>
- 553 Ryan, W. B. F., Carbotte, S. M., Coplan, J. O., O’Hara, S., Melkonian, A., Arko, R., et al.  
554 (2009). Global Multi-Resolution Topography synthesis. *Geochemistry, Geophysics,*  
555 *Geosystems*, 10(3), Q03014. <https://doi.org/10.1029/2008GC002332>
- 556 Sandvol, E., Seber, D., Calvert, A., & Barazangi, M. (1998). Grid search modeling of receiver  
557 functions: Implications for crustal structure in the Middle East and North Africa. *Journal*  
558 *of Geophysical Research: Solid Earth*, 103(B11), 26899–26917.  
559 <https://doi.org/10.1029/98JB02238>
- 560 Schilling, M. E., Carlson, R. W., Tassara, A., Conceição, R. V., Bertotto, G. W., Vásquez, M., et  
561 al. (2017). The origin of Patagonia revealed by Re-Os systematics of mantle xenoliths.  
562 *Precambrian Research*, 294, 15–32. <https://doi.org/10.1016/j.precamres.2017.03.008>
- 563 Schimmel, M., & Gallart, J. (2007). Frequency-dependent phase coherence for noise suppression  
564 in seismic array data. *Journal of Geophysical Research: Solid Earth*, 112(B4).  
565 <https://doi.org/10.1029/2006JB004680>
- 566 Schimmel, M., Stutzmann, E., & Gallart, J. (2011). Using instantaneous phase coherence for  
567 signal extraction from ambient noise data at a local to a global scale: Ambient noise  
568 signal extraction. *Geophysical Journal International*, 184(1), 494–506.  
569 <https://doi.org/10.1111/j.1365-246X.2010.04861.x>
- 570 Shen, W., Ritzwoller, M. H., Schulte-Pelkum, V., & Lin, F.-C. (2013). Joint inversion of surface  
571 wave dispersion and receiver functions: a Bayesian Monte-Carlo approach. *Geophysical*  
572 *Journal International*, 192(2), 807–836. <https://doi.org/10.1093/gji/ggs050>
- 573 Shen, W., Ritzwoller, M. H., Kang, D., Kim, Y., Lin, F.-C., Ning, J., et al. (2016). A seismic  
574 reference model for the crust and uppermost mantle beneath China from surface wave  
575 dispersion. *Geophysical Journal International*, 206(2), 954–979.  
576 <https://doi.org/10.1093/gji/ggw175>
- 577 Shibutani, T., Ueno, T., & Hirahara, K. (2008). Improvement in the Extended-Time Multitaper  
578 Receiver Function Estimation Technique. *Bulletin of the Seismological Society of*  
579 *America*, 98(2), 812–816. <https://doi.org/10.1785/0120070226>
- 580 Stacey, F. D., & Davis, P. M. (2008). *Physics of the Earth*. Cambridge University Press.
- 581 Stern, C. R., & Kilian, R. (1996). Role of the subducted slab, mantle wedge and continental crust  
582 in the generation of adakites from the Andean Austral Volcanic Zone. *Contributions to*  
583 *Mineralogy and Petrology*, 123(3), 263–281. <https://doi.org/10.1007/s004100050155>
- 584 Thorkelson, D. J. (1996). Subduction of diverging plates and the principles of slab window  
585 formation. *Tectonophysics*, 255(1–2), 47–63. [https://doi.org/10.1016/0040-](https://doi.org/10.1016/0040-1951(95)00106-9)  
586 [1951\(95\)00106-9](https://doi.org/10.1016/0040-1951(95)00106-9)
- 587 Thorkelson, D. J., & Breitsprecher, K. (2005). Partial melting of slab window margins: genesis  
588 of adakitic and non-adakitic magmas. *Lithos*, 79(1–2), 25–41.  
589 <https://doi.org/10.1016/j.lithos.2004.04.049>

- 590 Wiens, D. A., Robertson, S., Smith, G. P., Shore, P., Vera, E., Barrientos, S., et al. (1998).  
591 Seismic Experiment in Patagonia and Antarctica (SEPA). *IRIS Newsletter*, 17(1), 9–11.
- 592 Wiens, D. A., Mansour, W. B., Mark, H. F., Shore, P., Richter, A., & Barrientos, S. (2021).  
593 Geodynamics of the Patagonian Slab Window constrained by Shear Wave Splitting and  
594 Seismic Imaging. Presented at the AGU Fall Meeting, Earth and Space Science Open  
595 Archive. <https://doi.org/10.1002/essoar.10509443.1>
- 596 Withers, M., Aster, R., Young, C., Beiriger, J., Harris, M., Moore, S., & Trujillo, J. (1998). A  
597 Comparison of Select Trigger Algorithms for Automated Global Seismic Phase and  
598 Event Detection. *Bulletin of the Seismological Society of America*, 88(1), 12.
- 599 Wu, P., Wang, H., & Steffen, H. (2013). The role of thermal effect on mantle seismic anomalies  
600 under Laurentia and Fennoscandia from observations of Glacial Isostatic Adjustment.  
601 *Geophysical Journal International*, 192(1), 7–17. <https://doi.org/10.1093/gji/ggs009>
- 602 Zhu, L., & Kanamori, H. (2000). Moho depth variation in southern California from teleseismic  
603 receiver functions. *Journal of Geophysical Research: Solid Earth*, 105(B2), 2969–2980.  
604 <https://doi.org/10.1029/1999JB900322>  
605  
606  
607



*Geophysical Research Letters*

Supporting Information for

**Lithospheric Erosion in the Patagonian Slab Window, and Implications for Glacial Isostasy**

Hannah F. Mark<sup>1</sup>, Douglas A. Wiens<sup>1</sup>, Erik R. Ivins<sup>2</sup>, Andreas Richter<sup>3</sup>, Walid Ben Mansour<sup>1</sup>,  
M. Beatrice Magnani<sup>4</sup>, Eric Marderwald<sup>3</sup>, Rodrigo Adaros<sup>5</sup>, Sergio Barrientos<sup>6</sup>

<sup>1</sup>Department of Earth and Planetary Sciences, Washington University in St. Louis; <sup>2</sup>Jet Propulsion Laboratory, California Institute of Technology; <sup>3</sup>Laboratorio MAGGIA, Universidad Nacional de La Plata; CONICET;

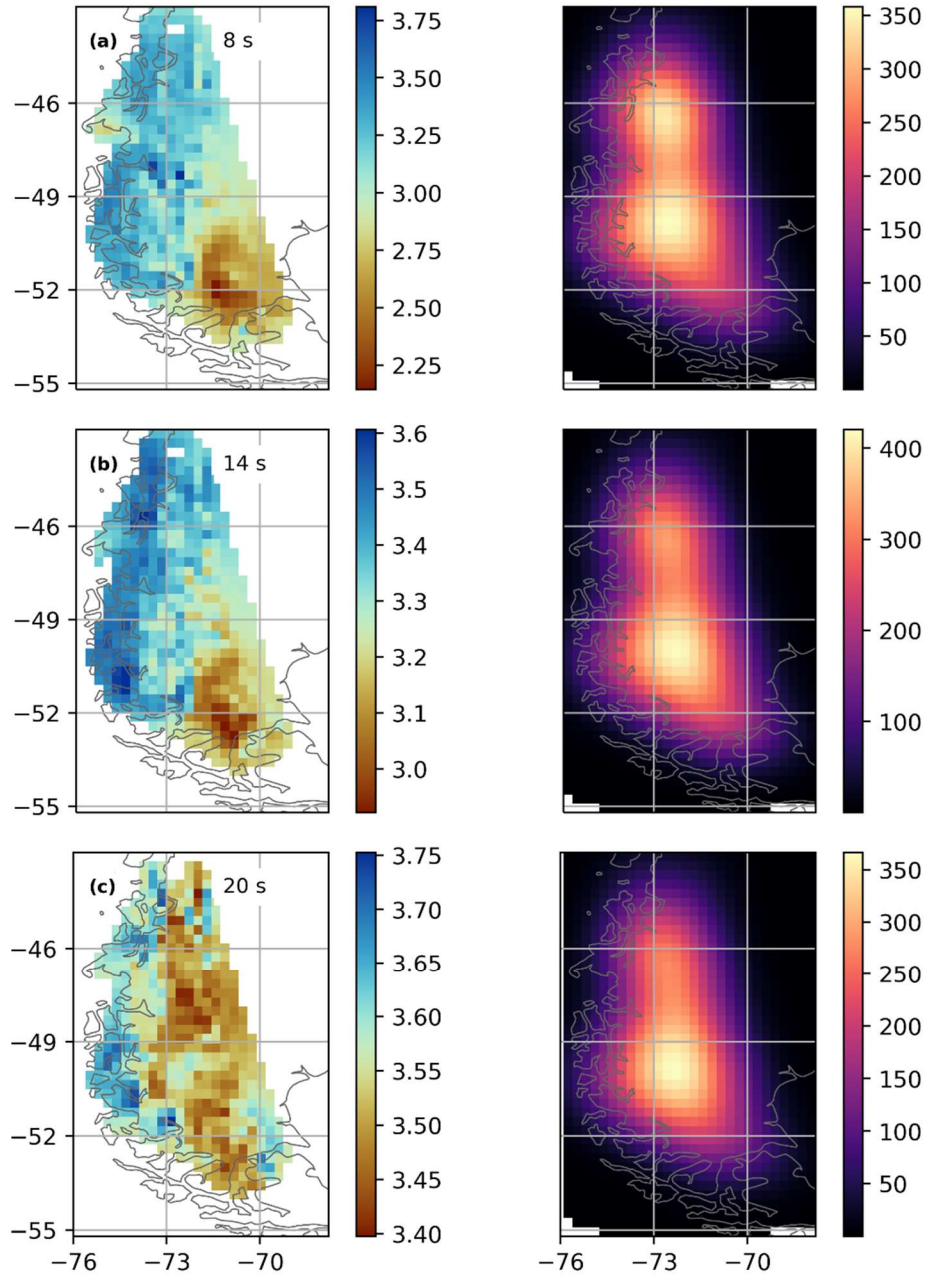
<sup>4</sup>Southern Methodist University; <sup>5</sup>Empresa Nacional del Petróleo, Magallanes; <sup>6</sup>Centro Sismológico Nacional, Universidad de Chile

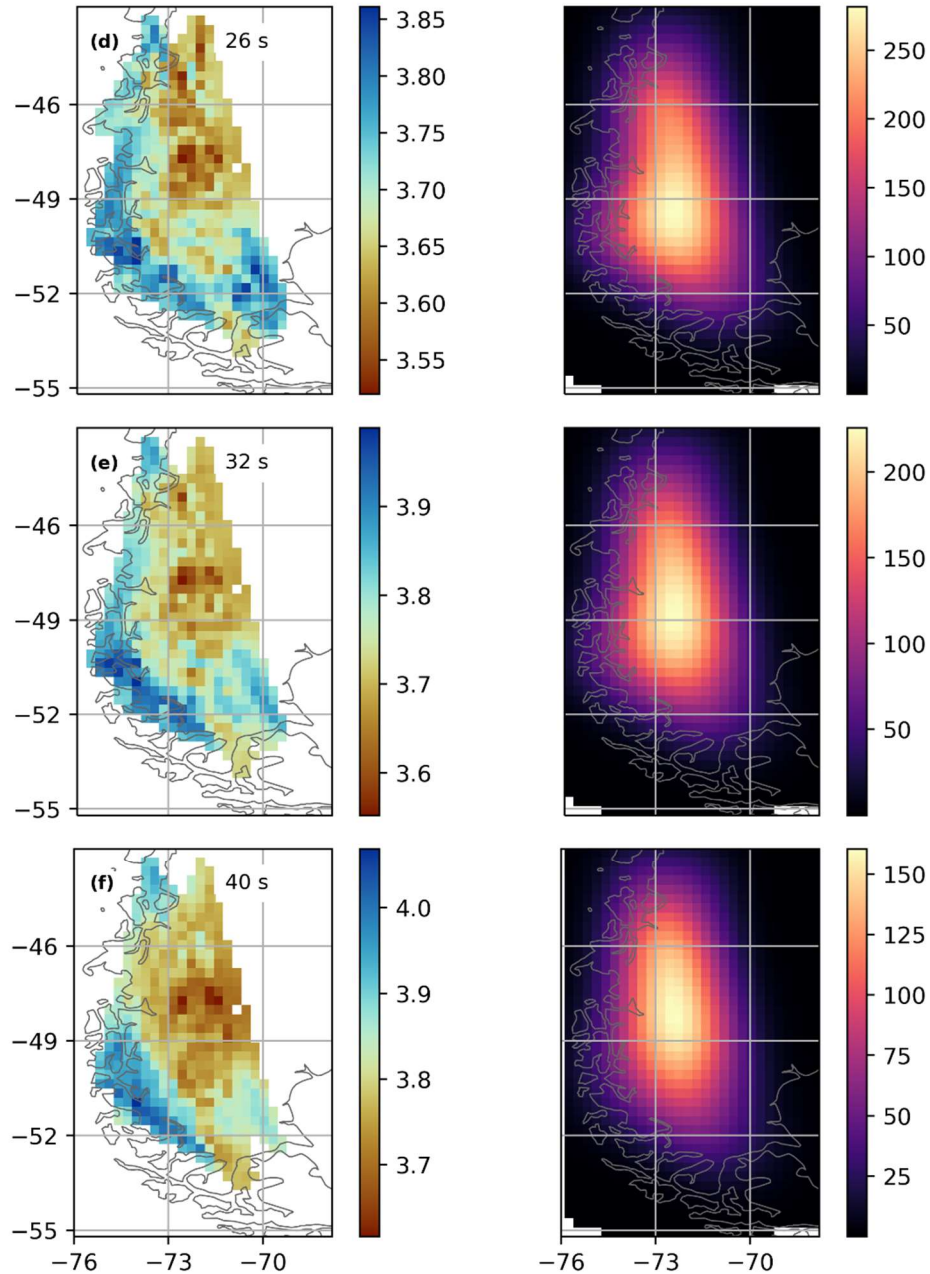
**Contents of this file**

Figures S1 to S8  
Table S1

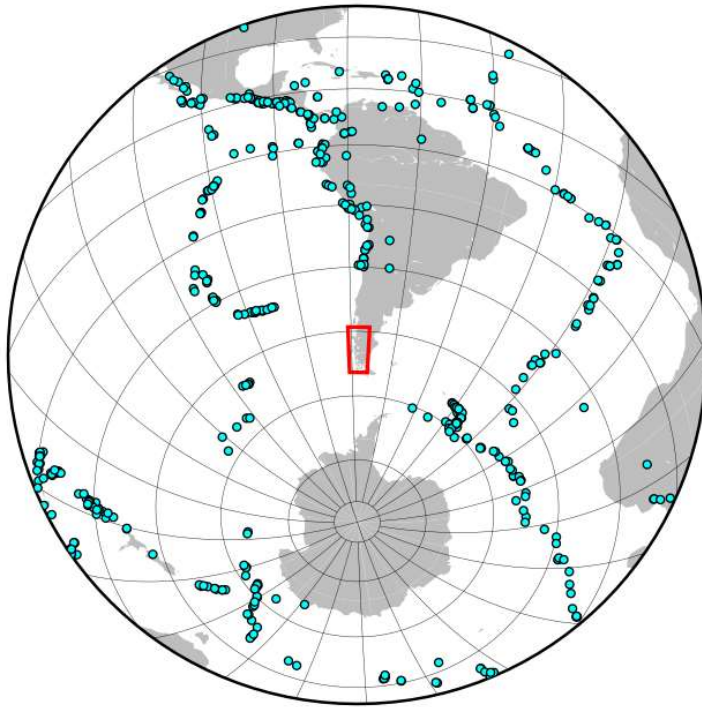
**Introduction**

This file contains supplemental figures and a table detailing parameters used for Bayesian inversion.

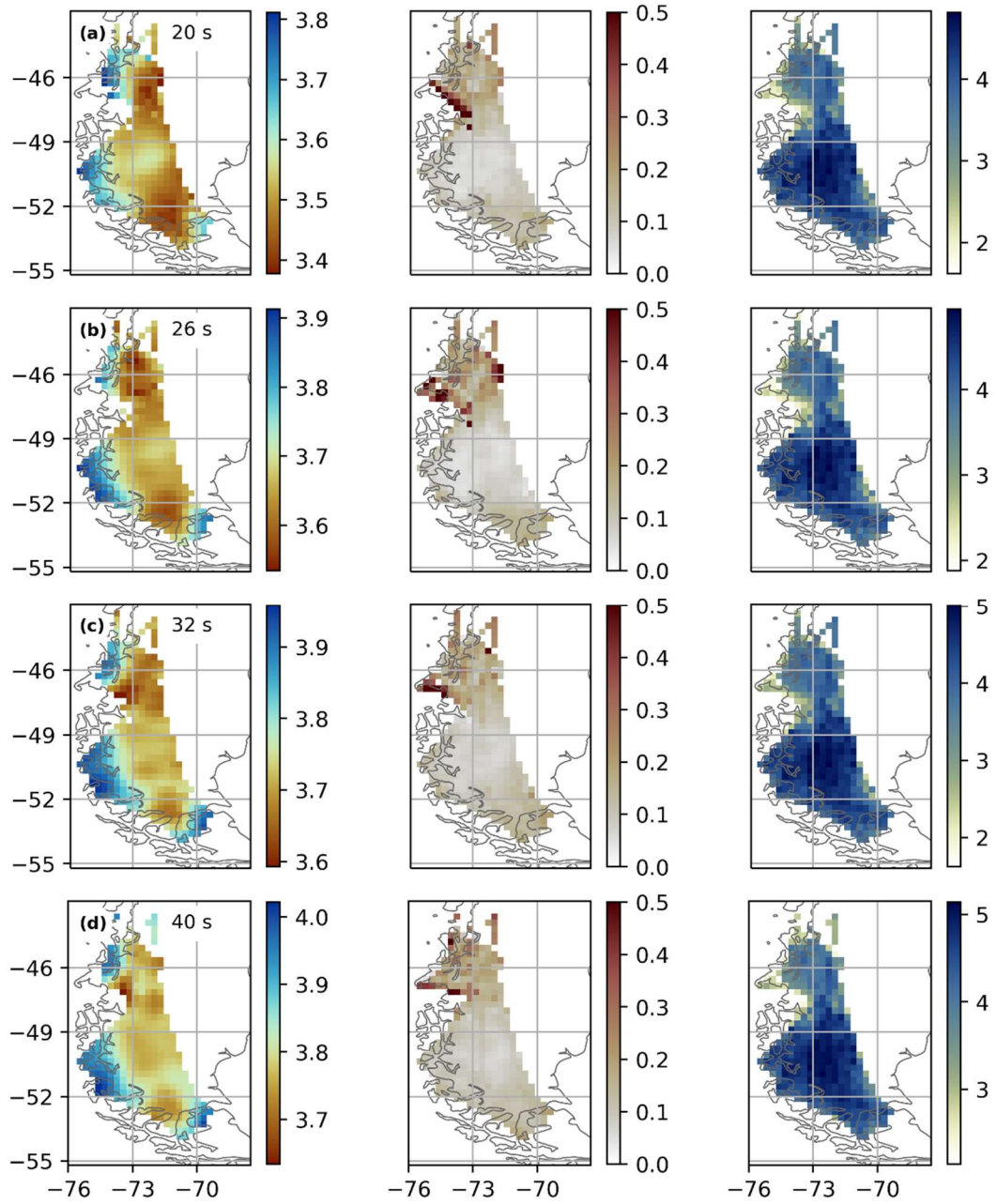




**Figure S1. Phase velocity maps from ambient noise tomography.** The left column shows phase velocities in km/s, and the right column shows path density smoothed over the map. Phase velocities are shown at periods of (a) 8 seconds, (b) 14 seconds, (c) 20 seconds, (d) 26 seconds, (e) 32 seconds, and (f) 40 seconds. Velocities are only shown where path density is greater than 10 and the resolution length scale is greater than 0.02.



**Figure S2. Event distribution map.** Blue dots mark the locations of earthquakes used for tomography. The study region is outlined by a red box.



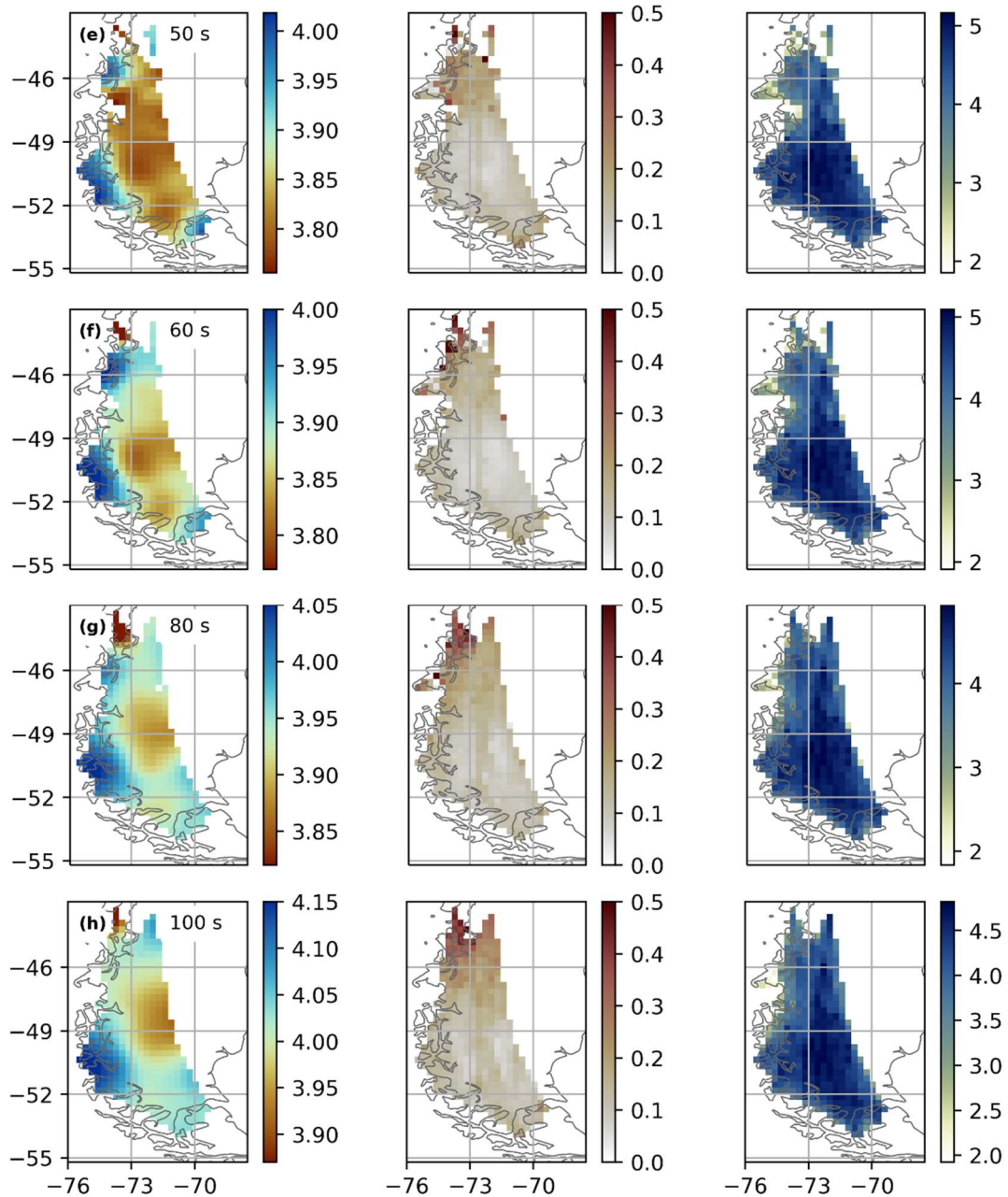


**Figure S3. Phase velocity maps from earthquake tomography.** The left column shows Helmholtz-corrected phase velocities in km/s, the middle column shows one standard deviation (in km/s) of the velocities calculated from stacking maps for each earthquake, and the right column shows  $\log_{10}$  of the number of paths used in each grid cell. Phase velocities are shown at periods of (a) 20 seconds, (b) 26 seconds, (c) 32 seconds, (d) 40 seconds, (e) 50 seconds, (f) 60 seconds, (g) 80 seconds, and (h) 100 seconds. Velocities are only shown for grid cells where velocity measurements were obtained for at least 10 events.

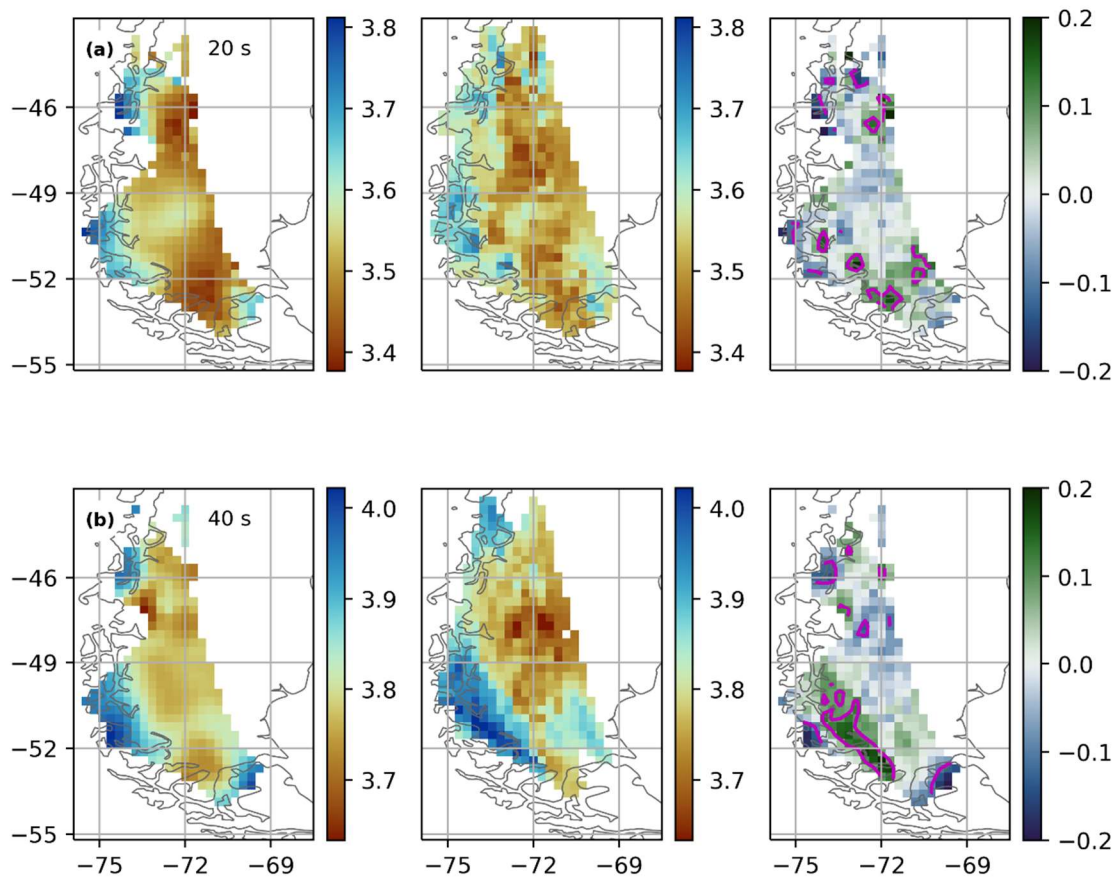


**Figure S4. Comparison between earthquake and ambient noise tomography.** The left column shows earthquake phase velocities as in Figure S3, the middle column shows ambient noise phase velocities as in Figure S1, and the right column shows the difference between the two velocity maps at **(a)** 20 seconds, and **(b)** 40 seconds. All velocities and velocity differences are in km/s. For the maps of velocity differences, magenta contours outline regions where the difference between the two velocity maps is greater than 0.1 km/s.

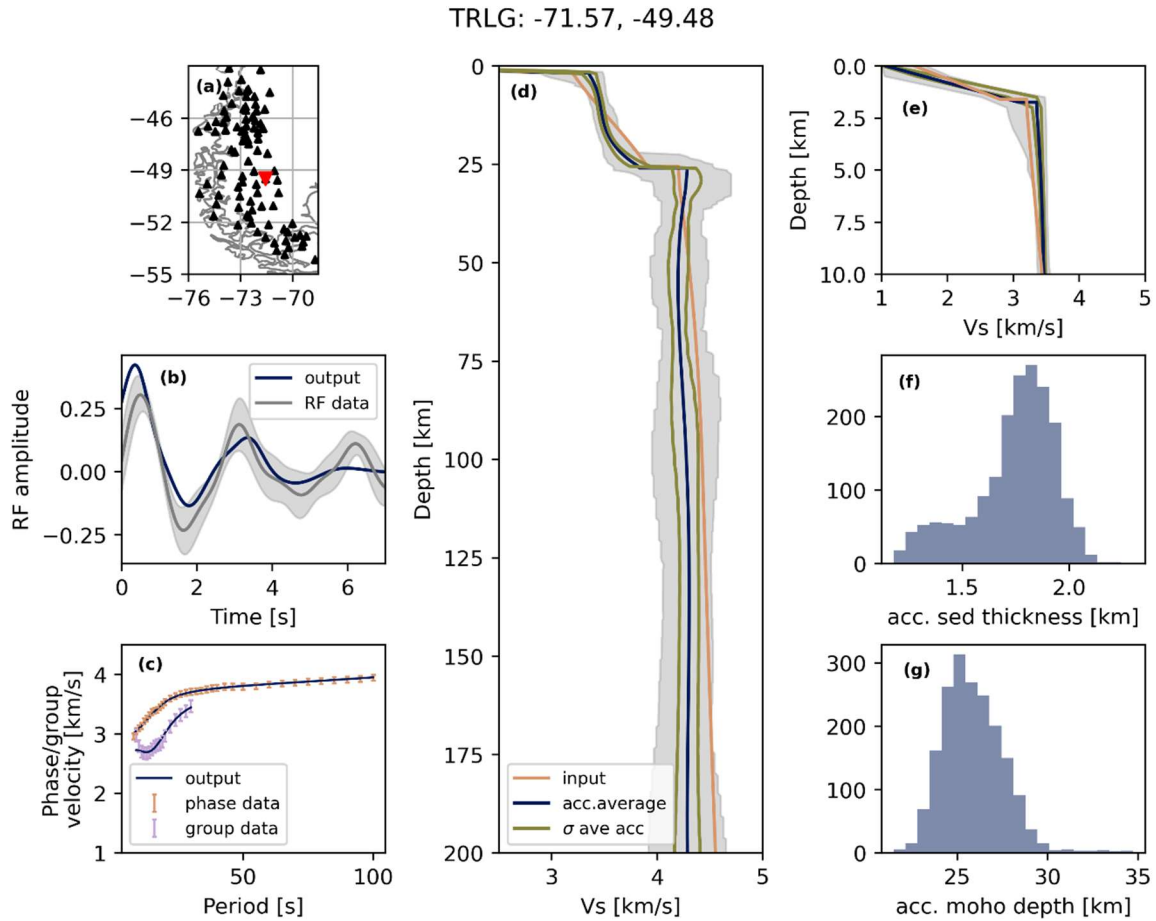


**Figure S5. Inversion results for station TRLG.** (a) Map showing station locations (black triangles) and the location of station TRLG (red inverted triangle). (b) Input station receiver function (grey line and shading) plotted with the forward-calculated receiver function for the average of all accepted velocity models for this station (dark blue line). (c) Input group and phase velocity measurements (pink and orange errorbars) with forward-calculated dispersion curves for the average of all accepted velocity models for this station (navy lines). (d) Inversion results to 200 km depth, showing the model for the centroid of the parameter prior distributions (orange line), the average of all accepted models (dark blue line), one standard deviation of all accepted models (green lines), and the range spanned by all accepted models (grey shading). (e) Shallow structure of accepted velocity models, with the same lines as in (d). (f) Histogram showing the distribution of sediment thicknesses for all accepted models. (g) Histogram showing the distribution of Moho depths for all accepted models.

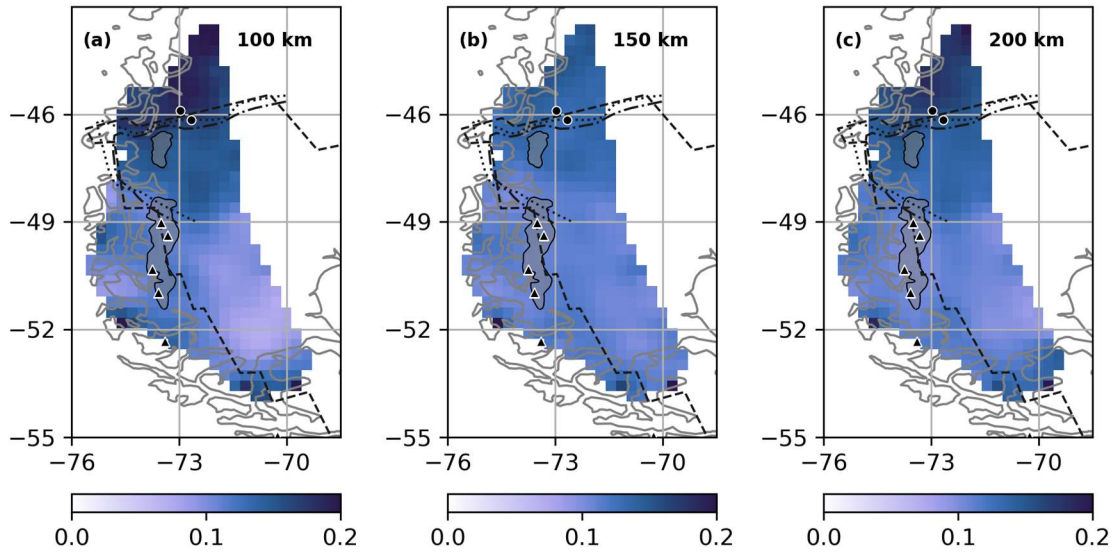


**Figure S6. Velocity uncertainty maps.** Maps show one standard deviation for  $V_{sv}$  (in km/s) at **(a)** 50 km, **(b)** 100 km, and **(c)** 150 km depth. The uncertainty maps correspond to the velocity depth slices shown in Figure 2 of the main text. On all maps, previously estimated slab window extents are shown from Russo et al. (2010) at depths of 50 km (dot-dashed line) and 100 km (dotted line), and from Breitsprecher and Thorkelson (2009) (dashed line)<sup>1,17</sup>. The present-day NPI and SPI are shaded in grey, and the locations of volcanoes are marked with black triangles (adakitic) and black circles (basaltic).

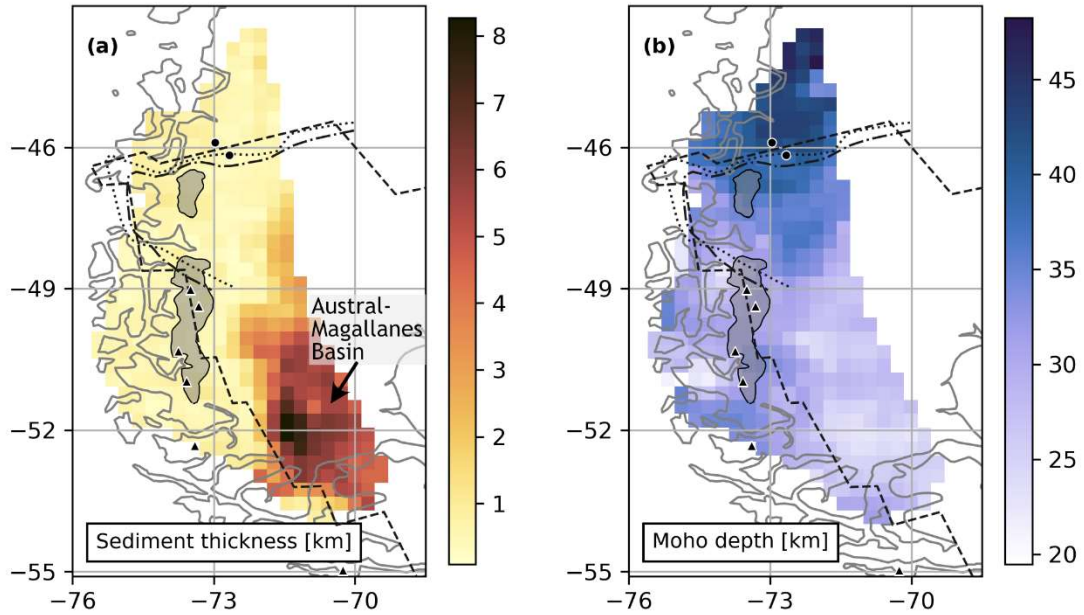


**Figure S7. Sediment thickness and Moho depth from the velocity model.** Maps of (a) sediment layer thickness and (b) Moho depth (sediments plus crust) show thick sediments in the Austral-Magallanes basin to the south, and a north-to-south decrease in crustal thickness across the study region. Features marked on the maps, including slab window outlines from previous studies, locations of volcanoes, and present-day icefield extents, are the same as in Figure 1. Uncertainty maps for interface depths are shown in Figure S8.

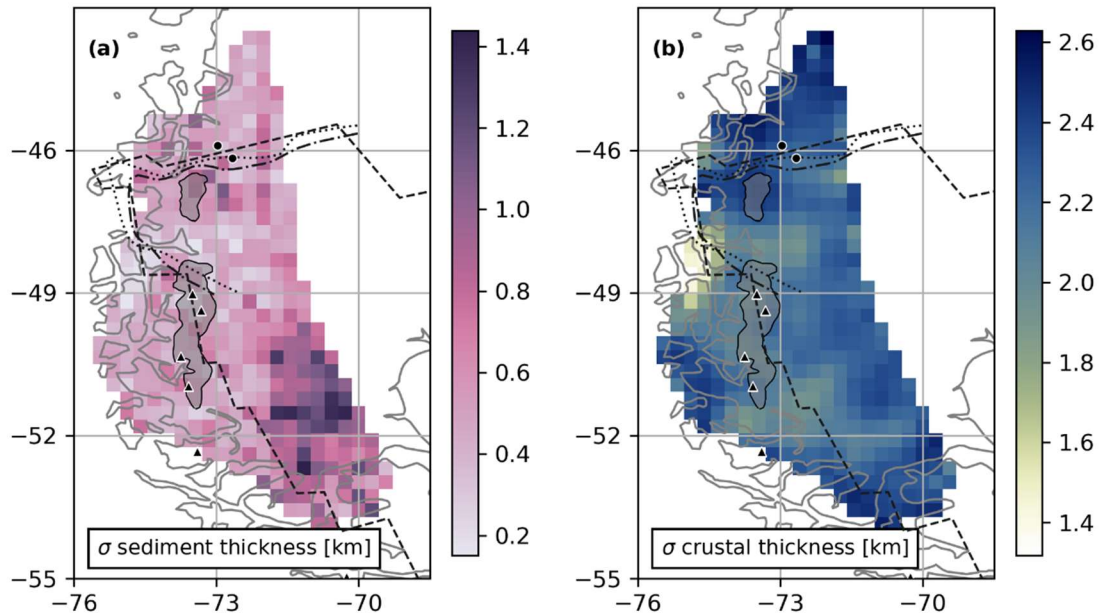


**Figure S8. Sediment thickness and crustal thickness uncertainty maps.** Maps show one standard deviation of **(a)** the sediment layer thickness, and **(b)** the crustal thickness, excluding sediments. Features marked on the maps, including slab window outlines from previous studies, locations of volcanoes, and present-day icefield extents, are the same as in Figure 1.

	<b>Layer type</b>	<b>Parameter</b>	<b>Value</b>	<b>Perturbation range</b>
<b>Sediments</b>	Gradient	Thickness ( $T_{\text{segs}}$ )	1 or 4 km	$\pm 1$ or 4 km
		Top velocity	1.5 km/s	$\pm 0.5$ km/s
		Bottom velocity	2.2 or 2.8 km/s	$\pm 0.6$ km/s
<b>Crust</b>	Cubic splines	Thickness ( $T_{\text{crust}}$ )	From H-k stacks	$\pm 9$ km
		1 <sup>st</sup> spline coeff.	3.2 km/s	$\pm 25\%$
		2 <sup>nd</sup> spline coeff.	3.4 km/s	$\pm 25\%$
		3 <sup>rd</sup> spline coeff.	3.6 km/s	$\pm 25\%$
		4 <sup>th</sup> spline coeff.	3.9 km/s	$\pm 25\%$
<b>Mantle</b>	Cubic splines	Thickness	$300 \text{ km} - T_{\text{crust}} - T_{\text{segs}}$	
		1 <sup>st</sup> spline coeff.	4.2 km/s	$\pm 25\%$
		2 <sup>nd</sup> spline coeff.	4.3 km/s	$\pm 25\%$
		3 <sup>rd</sup> spline coeff.	4.4 km/s	$\pm 25\%$
		4 <sup>th</sup> spline coeff.	4.5 km/s	$\pm 25\%$
		5 <sup>th</sup> spline coeff.	4.6 km/s	$\pm 25\%$
		6 <sup>th</sup> spline coeff.	4.7 km/s	Held constant

**Table S1.** Prior parameter distributions for Bayesian inversion.